The Astrophysical Journal, 902:85 (14pp), 2020 October 10 https://doi.org/10.3847/1538-4357/abb313

Hydrodynamic Winds from Twin-star Binaries

Morgan MacLeod and Abraham Loeb
Center for Astrophysics, Harvard & Smithsonian, 60 Garden Street, Cambridge, MA 02138, USA; morgan.macleod@cfa.harvard.edu
Received 2020 July 14; revised 2020 August 25; accepted 2020 August 26; published 2020 October 14

Abstract

Stellar winds shape the evolution of stars through the loss of mass. In binary systems, they also shape the stars' evolution by modifying the orbit. In this paper, we use hydrodynamic simulations to study the emergence of nearly isothermal winds from identical twin binaries. We vary the degree to which model stars fill their Roche lobes and the temperature of the wind. Initialized at rest on the stellar surfaces, winds accelerate away from the binary components through a sonic surface to supersonic outward velocities. In cases where the binary fills its Roche lobe, a shared subsonic region surrounds both components. We find that mass loss rates from close twin-star binaries are enhanced relative to the expectation from two single-object winds. This binary enhancement is best modeled as a function of the ratio of wind velocity to orbital velocity. Similarly, we find that the specific angular momentum with which winds emerge can vary between that of the binary components and that of the outer Lagrange points depending on the ratio of wind velocity to orbital velocity. Given that mass and angular momentum loss can be modeled as simple functions of wind velocity, our results may be broadly applicable to the evolution of close, equal-mass binaries. One particularly important potential application is to massive, close binaries, which may be progenitors of binary black hole mergers through the chemically homogeneous evolution channel.

Unified Astronomy Thesaurus concepts: Binary stars (154); Close binary stars (254); Stellar winds (1636); Hydrodynamics (1963)

Supporting material: figure sets

1. Introduction

Many stars exist in binary or multiple systems (Duchêne & Kraus 2013). Among these, massive stars are particularly likely to be found in close pairs of similar mass objects (Sana et al. 2012; de Mink et al. 2014). One such example is the over-contact pair VFTS352, which is composed of two approximately $29M_{\odot}$ components that fill their mutual Roche lobes (Almeida et al. 2015). Sources like these are of significant interest as potential progenitor systems of binary compact object remnants that can inspiral and merge through the emission of gravitational radiation (de Mink & Mandel 2016; Mandel & de Mink 2016; Marchant et al. 2016; Song et al. 2016). In these systems, rotation assists internal mixing and leads much of the stellar hydrogen to be burned and incorporated into the compact core (de Mink et al. 2009), which later collapses.

Stars ubiquitously lose mass via winds from their surfaces. Depending on the stellar type, the wind-acceleration mechanism and thermal properties can differ, and may depend on stellar metallicity or magnetic field (Lamers & Cassinelli 1999). Wind mass loss significantly modifies the evolution of stars and shapes the distribution of stellar remnant masses (e.g., Spera et al. 2015). When stars are in binary or multiple systems, wind mass and angular momentum losses have the further effect of transforming the binary orbit. The details of how much mass stars lose, and the specific angular momentum with which it is expelled from a binary system, are therefore crucial for understanding the details of how stellar winds affect evolving binary systems (e.g., Lin 1977; Savonije 1983; Tout & Hall 1991; Brookshaw & Tavani 1993; Hurley et al. 2002; Chen et al. 2018).

In close binaries, stellar winds interact with each other and with the combined gravitational effective potential of the pair. Although a variety of approaches have been used, some of the most informative models of this process come from hydrodynamic simulations. Much of this work has focused on the dynamics of stellar wind capture by companion objects (e.g., Blondin et al. 1990, 1991; Taam et al. 1991; Theuns & Jorissen 1993; Blondin 1994; Blondin & Woo 1995; Theuns et al. 1996; Nagae et al. 2004; Jahanara et al. 2005; Mohamed & Podsiadlowski 2007; de Val-Borro et al. 2009, 2017; Bosch-Ramon et al. 2012; Huarte-Espinosa et al. 2013; Čechura & Hadrava 2015; El Mellah et al. 2018, 2019, 2020; Saladino & Pols 2019; Tomaru et al. 2019; Xu & Stone 2019; Bermúdez-Bustamante et al. 2020), which is of particular observational importance for X-ray binaries in which the accretor is a compact object. Other hydrodynamic modeling, also motivated by X-ray observations, has focused on the morphology and dynamics of colliding winds in binaries with pairs of wind-emitting stars, such as Wolf–Rayet binaries (e.g., Stevens et al. 1992; Owocki & Gayley 1995; Pittard 1998, 2007, 2009; Walder 1998; Lemaster et al. 2007; Parkin & Pittard 2008; Lamberts et al. 2011, 2012, 2013; Parkin & Gosset 2011; Parkin et al. 2011, 2014; van der Helm et al. 2019).

In the following we study the morphology of thermally driven stellar winds, similar to the Parker (1958) solar wind model, in close pairs of stars. We focus on equal-mass systems, with identical surface conditions, and we examine how the degree of Roche-lobe occupancy (how close the system is to filling its Roche lobes) and the stellar-surface sound speed affect the emergent winds. We measure rates of mass and angular momentum loss from the binary system and compare these to analytic predictions for single and binary systems.

The paper is organized as follows. In Section 2, we describe our hydrodynamic simulation method. In Section 4, we describe our numerical results and discuss their interpretation. In Section 5, we discuss potential limitations of our results and their broader applicability to astrophysical binaries with various

wind-acceleration mechanisms. Finally, in Section 6, we conclude.

2. Simulation Method and Models

Our simulation model is composed of two identical stellar components, whose surfaces are in corotation with the binary orbit. We simulate the interaction of hydrodynamic winds launched from these surfaces. Our models are developed using the `Athena++` code (Stone et al. 2020),[1] which is a Eulerian (magneto) hydrodynamic code descended from `Athena` (Stone et al. 2008).

The total mass of the binary is M, and the mass of each of the individual components is $M_1 = M_2 = M/2$. The separation of their circular orbit is a. Our models are performed in units where $G = M = a = 1$. This implies that the unit velocity is $\sqrt{GM/a} = 1$, and the unit time is $\sqrt{a^3/GM} = 1$, such that the orbital period is $P_{\rm orb} = 2\pi$.

2.1. Computational Method

We solve the equations of inviscid gas dynamics in a frame of reference centered on the binary center of mass rotating with the binary orbital frequency $\Omega = \sqrt{GM/a^3}$. We employ a Cartesian mesh, with nested levels of static mesh refinement surrounding the binary components.

The conservation equations that we solve are

$$\partial_t \rho + \nabla \cdot (\rho \boldsymbol{v}) = 0, \tag{1a}$$

$$\partial_t (\rho \boldsymbol{v}) + \nabla \cdot (\rho \boldsymbol{v}\boldsymbol{v} + P\boldsymbol{I}) = -\rho \boldsymbol{a}_{\rm ext}, \tag{1b}$$

$$\partial_t E + \nabla \cdot [(E + P)\boldsymbol{v}] = -\rho \boldsymbol{a}_{\rm ext} \cdot \boldsymbol{v}, \tag{1c}$$

expressing mass continuity, the evolution of gas momenta, and the evolution of gas energies. In the above equations, ρ is the mass density, $\rho\boldsymbol{v}$ is the momentum density, and $E = \epsilon + \rho\boldsymbol{v}\cdot\boldsymbol{v}/2$ is the total energy density with ϵ being the internal energy density. The pressure is P, $\boldsymbol{I}$ is the identity tensor, and $\boldsymbol{a}_{\rm ext}$ is the acceleration associated with the binary and the rotating frame of reference. These equations are closed by an ideal gas equation of state, $P = (\gamma - 1)\epsilon$, where γ is the gas adiabatic index.

The source terms of the binary's gravity and rotating reference frame are contained in the acceleration,

$$\boldsymbol{a}_{\rm ext} = -\frac{GM_1}{|\boldsymbol{r}_1|^3}\boldsymbol{r}_1 - \frac{GM_2}{|\boldsymbol{r}_2|^3}\boldsymbol{r}_2 - \boldsymbol{\Omega}\times\boldsymbol{\Omega}\times\boldsymbol{r} - 2\boldsymbol{\Omega}\times\boldsymbol{v}, \tag{2}$$

where $\boldsymbol{r_i}$ is the vectorial separation between a zone and the center of star i, $\boldsymbol{\Omega} = (0, 0, \Omega)$ is the vectorial orbital frequency, and r and v are the position and velocity relative to the center of mass of the rotating reference frame (i.e., the position and velocity in the computational domain). Thus, the (x, y) coordinates define the binary orbital plane. There is no gravitational backreaction of the wind distribution on the binary.

The boundary of the stellar surfaces is chosen by a value, $\Phi_{\rm s}$, of the gravitational effective potential,

$$\Phi_{\rm eff} = -\frac{GM_1}{r_1} - \frac{GM_2}{r_2} - \frac{1}{2}\Omega^2 R^2, \tag{3}$$

where $R = \sqrt{x^2 + y^2}$. In regions close to M_1 or M_2 where $\Phi_{\rm eff} < \Phi_{\rm s}$, we set the gas velocities to zero and remove any acceleration terms. The density and pressure are set to fixed stellar "surface" values of $\rho_{\rm s}$ and $p_{\rm s}$. We set the surface density[2] to $\rho_{\rm s} = 1M/a^3$. The pressure is based on the hydrodynamic escape parameter,

$$\lambda = -\frac{\Phi_{\rm s}}{c_{\rm s,s}^2}, \tag{4}$$

where $c_{\rm s,s}^2 = \gamma p_{\rm s}/\rho_{\rm s}$ is the squared sound speed of the stellar surface. Thus,

$$p_{\rm s} = -\frac{\rho_{\rm s}\Phi_{\rm s}}{\gamma\lambda}. \tag{5}$$

We specify the value of $\Phi_{\rm s}$ by comparison to $\Phi_{\rm eff}$ at the L_1 Lagrange point, which, in the case of $M_1/M_2 = 1$, is located at the center of mass,

$$\Phi_{\rm s} = f_\Phi\,\Phi_{\rm eff}(L_1) = -2f_\Phi, \tag{6}$$

where the second equality holds with our chosen masses and code units.

The simulation domain extends to $\pm 48a$ in each direction from the center of mass, located at the origin. The base mesh is composed of 256^3 zones. We nest five additional levels of static mesh refinement interior to this base mesh, each containing 256^3 zones, for example, the region within ± 24 is refined one level, within ± 12 two levels, up to ± 1.5 refined five times. The smallest zone sizes are cubes with sides of $3/256 \approx 0.0117$. This mesh is decomposed into meshblocks of 16^3 zones each. The outer boundary conditions in each direction are "outflow," extending the conditions interior to the domain to the ghost zones.

2.2. Models

We run a suite of models varying λ and f_Φ. For the adiabatic index, we adopt the nearly isothermal value $\gamma = 1.01$. We set $\lambda = 2.5$, 5.0, and 10.0 with $f_\Phi = 1$, $\sqrt{2}$, 2, and 4. In the following we discuss these 12 parameter combinations of λ and f_Φ.

3. Analysis Metrics

3.1. Mass and Angular Momentum Loss

We measure the mass loss rate from the binary via a surface integral,

$$\dot{M} = -\oint_S \rho(\boldsymbol{v}\cdot\boldsymbol{dA}), \tag{7}$$

surrounding the binary. In practice, we perform this integral by summing across the outward faces, $\boldsymbol{dA}$, of zones closest to a sphere, S, surrounding the center of mass. We adopt a radius of $5a$ to define S in the following, but have confirmed that our results would be nearly constant for any choice of radius between $2a$ and $6a$. The flux of the $\hat{z}$-component of angular

[1] Version 2019, https://princetonuniversity.github.io/athena.

[2] Setting $\rho_{\rm s}$ has the effect of normalizing the mass loss rate. Because we do not include any backreaction on the binary orbit or any density-dependent heating or cooling physics, this parameter can be defined independently of the other choices of units.

momentum through this surface is similarly measured as

$$\dot{L} = \dot{\boldsymbol{L}} \cdot \hat{z} = -\oint_S \rho(\boldsymbol{r} \times \boldsymbol{v}) \cdot \hat{z}(\boldsymbol{v} \cdot \boldsymbol{dA}), \tag{8}$$

where quantities are measured in the inertial (nonrotating) frame. Because of the symmetry defined by the orbital plane, we find that the $\hat{x}$ and $\hat{y}$ components sum to zero to machine precision.

Combining these two fluxes, we define the specific angular momentum with which gas is lost from the binary,

$$l_{\rm loss} = \frac{\dot{L}}{\dot{M}}, \tag{9}$$

and its dimensionless counterpart, scaled to the specific angular momentum of the binary,

$$\gamma_{\rm loss} = \frac{l_{\rm loss}}{l_{\rm bin}}, \tag{10}$$

where $l_{\rm bin} = L/M = 1/4$. Thus, $\dot{L} = \dot{M} l_{\rm loss}$ and $L = M\, l_{\rm bin}$.

Angular momentum is acquired by the wind through a combination of the rotational motion of the binary about the center of mass, hydrodynamic stresses, and gravitational stresses. To understand this decomposition, it can be useful to separate these components.

The gravitational stress on the fluid within the volume enclosed by S implies a rate of change of the binary's angular moment that is equal and opposite to the torque on the wind from the binary,

$$\dot{L}_{\rm grav} = \dot{\boldsymbol{L}}_{\rm grav} \cdot \hat{z} = \int \sum_{i=1,2} (\boldsymbol{r_i} \times \boldsymbol{f}_{{\rm grav},i}) \cdot \hat{z}\ \rho dV, \tag{11}$$

where $\boldsymbol{r_i}$ is the position of binary component i, and

$$\boldsymbol{f}_{{\rm grav},i} = \frac{GM_i}{|\boldsymbol{r_i}|^3}\boldsymbol{r_i}, \tag{12}$$

is the gravitational force of the binary on the wind per unit mass. Without loss of generality, we choose the orientation of the binary to be along the x-axis, so that the integrand can be simplified to

$$\sum_{i=1,2} (\boldsymbol{r_i} \times \boldsymbol{f}_{{\rm grav},i}) \cdot \hat{z} = x_1 \frac{GM_1}{|\boldsymbol{r}_1|^3} y + x_2 \frac{GM_2}{|\boldsymbol{r}_2|^3} y, \tag{13}$$

where $x_1 = -1/2$ and $x_2 = 1/2$.

We define

$$l_{\rm grav} = -\frac{\dot{L}_{\rm grav}}{\dot{M}} \tag{14}$$

to describe the specific angular momentum imparted to the wind by torques from the binary and also define

$$\gamma_{\rm grav} = \frac{l_{\rm grav}}{l_{\rm bin}}. \tag{15}$$

Finally, we distinguish the portion of wind specific angular momentum not arising from gravitational torques as

$$l_{\rm wind} = l_{\rm loss} - l_{\rm grav} \tag{16}$$

and

$$\gamma_{\rm wind} = \frac{l_{\rm wind}}{l_{\rm bin}}, \tag{17}$$

such that the total $\gamma_{\rm loss}$ is the sum of the hydrodynamic (wind) and gravitational components, $\gamma_{\rm loss} = \gamma_{\rm wind} + \gamma_{\rm grav}$.

3.2. Wind Properties

In addition to typical hydrodynamic properties, we define two useful characteristics of the wind, the Jacobi and Bernoulli parameters. Each of these is invariant in certain circumstances —and analyzing these properties allows us to decompose the hydrodynamic and gravitational stresses acting on the wind.

The Jacobi parameter is

$$E_J = \frac{1}{2} v_{\rm rot}^2 + \Phi_{\rm eff}, \tag{18}$$

where $v_{\rm rot}$ is the magnitude of the velocity in the frame rotating with the binary. In the restricted three-body problem (Murray & Dermott 1999), test particles in the binary potential follow trajectories of a constant Jacobi parameter. A constant Jacobi parameter along wind trajectories thus indicates that material is expanding freely along ballistic trajectories. Variations in the Jacobi parameter indicate the importance of hydrodynamic stresses.

The Bernoulli parameter of material in the wind is

$$\mathcal{B} = \frac{1}{2} v^2 + \Phi + h, \tag{19}$$

where h is the fluid enthalpy,

$$h = \frac{\gamma}{\gamma - 1}\frac{P}{\rho}. \tag{20}$$

For material at rest in the rotating frame (as is the case for the surface boundary conditions of our model stars) $\mathcal{B}_{\rm s} = E_{J,s} + h = \Phi_{\rm s} + h$. These values are tabulated in Table 1. The Bernoulli parameter is constant along fluid streamlines, such as a freely expanding wind that does not self-intersect (e.g., Thompson 2006).

3.3. Binary Orbital Evolution

We begin with the expression for the orbital angular momentum of a binary system, $L = M_1 M_2 / M\sqrt{GMa}$. In our case $M_1 = M_2 = M/2$, so

$$L = \frac{1}{4}\sqrt{GM^3 a}. \tag{21}$$

By differentiating L with respect to time, then dividing by L, we find

$$\frac{\dot{a}}{a} = \frac{2\dot{L}}{L} - \frac{3\dot{M}}{M}. \tag{22}$$

Thus, measuring $\dot{M}$ and $\dot{L}$ allows us to estimate the separation evolution of the circular orbit.

Substituting in the definition of $\gamma_{\rm loss}$, the orbit evolution equation can be rewritten as

$$\frac{\dot{a}}{a} = (2\gamma_{\rm loss} - 3)\frac{\dot{M}}{M}, \tag{23}$$

where $\dot{M} < 0$, so $\gamma_{\rm loss} > 3/2$ implies that $\dot{a} < 0$, while $\gamma_{\rm loss} < 3/2$ implies that $\dot{a} > 0$. This can be rewritten as

$$\frac{d\ln a}{d\ln M} = 2\gamma_{\rm loss} - 3 \tag{24}$$

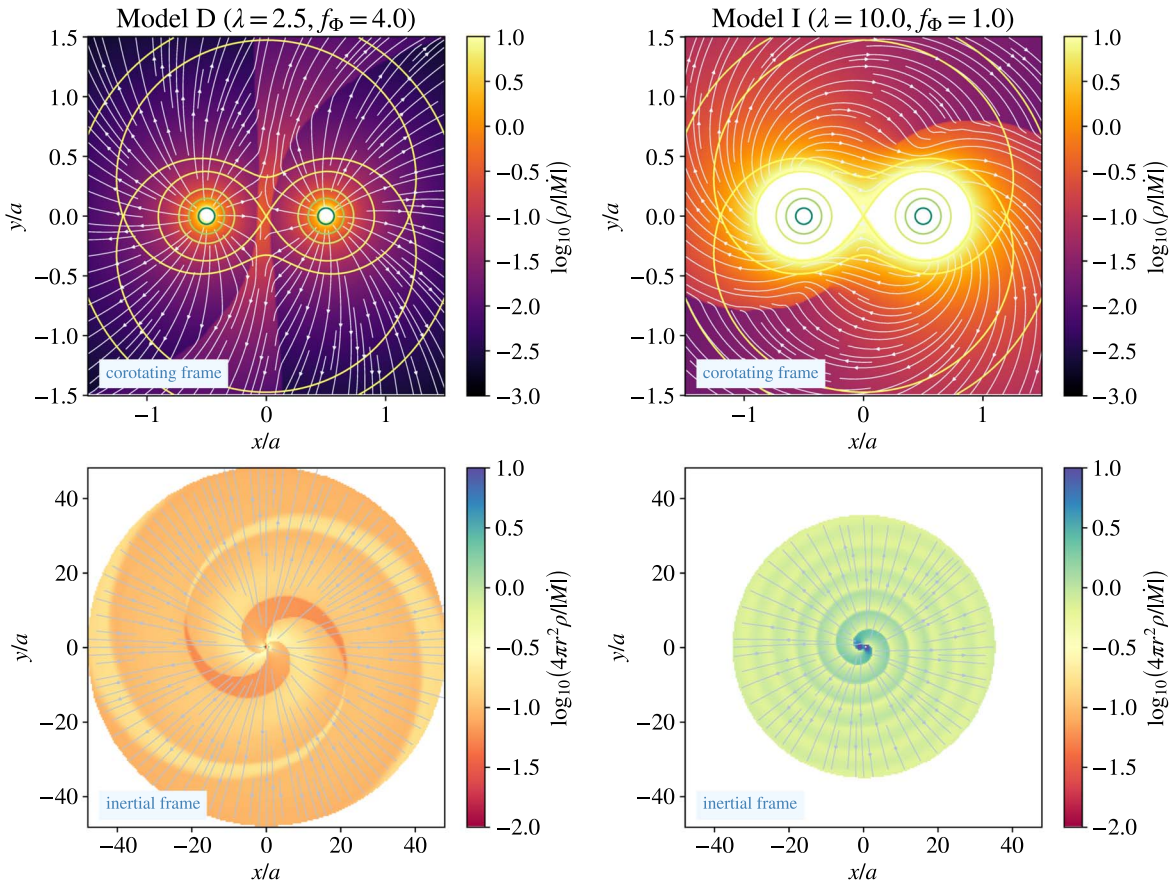

Figure 1. Slices of wind density normalized by mass loss rate (upper panels) and with the approximate r^{-2} scaling removed (lower panels). Note that the upper panels zoom-in on the region surrounding the binary, while the lower panels show a greater extent of the circumbinary environment. Streamlines in the upper panels are plotted in the corotating frame, while streamlines in the lower panels are shown in the inertial frame. Winds from the two components join and interact near the binary, before forming a largely spherical outflow with spiral disturbances on larger scales. The complete figure set (12 images) is available in the online journal and (MacLeod 2020).

(The complete figure set (12 images) is available.)

Table 1
Simulation Parameters and Results

Model	γ	λ	f_Φ	p_s	$c_{s,s}$	$E_{J,s}$	$\mathcal{B}_s$	$\dot{M}$	$\dot{L}$	$\dot{L}_{grav}$	γ_{loss}	γ_{wind}	γ_{grav}	v_{10}
A	1.01	2.5	1.00	0.79	0.89	−2.00	78.00	−1.17e+00	−3.85e−01	3.99e−02	1.31	1.45	−0.14	2.89
B	1.01	2.5	1.41	1.12	1.06	−2.83	110.31	−5.15e−01	−1.36e−01	1.24e−02	1.05	1.15	−0.10	3.64
C	1.01	2.5	2.00	1.58	1.26	−4.00	156.00	−2.57e−01	−6.56e−02	4.17e−03	1.02	1.09	−0.07	4.56
D	1.01	2.5	4.00	3.17	1.79	−8.00	312.00	−7.61e−02	−2.09e−02	2.90e−04	1.10	1.12	−0.02	7.03
E	1.01	5.0	1.00	0.40	0.63	−2.00	38.00	−5.15e−01	−2.15e−01	1.28e−02	1.67	1.77	−0.10	1.76
F	1.01	5.0	1.41	0.56	0.75	−2.83	53.74	−2.10e−01	−5.34e−02	1.32e−02	1.02	1.27	−0.25	2.22
G	1.01	5.0	2.00	0.79	0.89	−4.00	76.00	−1.07e−01	−2.10e−02	7.56e−03	0.79	1.07	−0.28	2.82
H	1.01	5.0	4.00	1.58	1.26	−8.00	152.00	−2.78e−02	−6.64e−03	3.39e−04	0.96	1.00	−0.05	4.49
I	1.01	10.0	1.00	0.20	0.45	−2.00	18.00	−7.47e−02	−6.41e−02	−1.69e−02	3.43	2.53	0.91	1.15
J	1.01	10.0	1.41	0.28	0.53	−2.83	25.46	−9.72e−03	−6.00e−03	−2.75e−03	2.47	1.34	1.13	1.39
K	1.01	10.0	2.00	0.40	0.63	−4.00	36.00	−2.76e−03	−1.14e−03	5.62e−05	1.66	1.74	−0.08	1.71
L	1.01	10.0	4.00	0.79	0.89	−8.00	72.00	−7.87e−04	−1.31e−04	2.51e−05	0.67	0.79	−0.13	2.73

Note. Model parameters include: γ, the gas adiabatic index, λ, the hydrodynamic escape parameter, f_Φ, the potential of the stellar surfaces relative to Φ_{L1}, p_s, and $c_{s,s}$ the pressure and sound speed of the stellar surface boundary condition, $E_{J,s}$ and $\mathcal{B}_s$, the surface Jacobi and Bernoulli parameters. Model results include $\dot{M}$, the total mass flux from the binary, $\dot{L}$, the total angular momentum flux away from the binary, $\dot{L}_{grav}$, the portion of $\dot{L}$ attributable to gravitational torques on the binary by the wind distribution. γ_{loss} is the dimensionless specific angular momentum of the wind, while γ_{wind} and γ_{grav} are the portions of this angular momentum attributable to hydrodynamic and gravitational stresses, respectively. Finally, v_{10} is the mean wind radial velocity at $r = 10a$. Model results are best converted to astrophysical units and applied to astrophysical systems through the dimensionless specific angular momenta γ_{loss}, γ_{wind}, and γ_{grav}, and through the comparison of $\dot{M}$ to analytic predictions, as approximated by Equation (29).

in terms of the orbital separation change per unit mass change. Integrated over some change in binary mass, the ratio of final to initial separation a_f/a_i depends on the ratio of final binary mass to initial mass, M_f/M_i,

$$\frac{a_f}{a_i} = \left(\frac{M_f}{M_i}\right)^{2\gamma_{\rm loss}-3}. \quad (25)$$

Thus, when $\gamma_{\rm loss} = 1$, this takes on the simple form, $a_f/a_i = M_i/M_f$.

4. Results

4.1. Twin Wind Morphology

The thermal winds in our model are accelerated from rest on the surfaces of the binary components by the pressure gradient established as the wind expands into the surrounding space. Figure 1 shows slices of density in the binary equatorial plane (the figure set online shows each of the models in Table 1). The upper panels show the density, normalized by the mass loss rate, in the region in the vicinity of the binary components with flow streamlines in the corotating frame. In the lower panels, we plot $4\pi r^2\rho/|\dot{M}|$ to visualize deviation from a spherically expanding constant radial velocity wind. In this panel, velocity streamlines are shown in the nonrotating inertial reference frame.

The wind density structures in the vicinity of the binary depend greatly upon the degree of contact of the binary components, parameterized by f_Φ and the hydrodynamic escape parameter λ. The influence of these parameters may be compared in Figure 1. For Model D, in which $\lambda = 2.5$ and $f_\Phi = 4$, the relatively high surface sound speed leads to rapidly expanding, supersonic winds. The separation of the binary relative to the component sizes leads the winds to establish separately prior to colliding in an interaction region. The rotation of the binary system imparts a spiral shape to this collision sheet (Lemaster et al. 2007). By contrast, Model I, for which $\lambda = 10$ and $f_\Phi = 1$, exhibits a dense circulating layer surrounding the binary. Material trails away from the binary system along the leading edges of the rotating pair, passing through the outer L_2 and L_3 Lagrange points (which have identical potential for our equal-mass case). Other models exhibit behavior intermediate between these extremes, with winds superimposing to form spiral structures emanating from the binaries' vicinity.

In examining the large-scale density and kinematic structures, we find that for each of our models the wind expands nearly radially in all directions (with $v_\phi \ll v_r$), and that wind densities reflect this nearly spherical expansion with an approximately $\rho \propto r^{-2}$ density structure. Deviations from this baseline behavior of a spherical wind represent differences relative to spherical expansion at constant velocity. Figure 1 shows that the binary's motion imparts spiral waves on the expanding winds. The winding angle of these waves depends on the normalization of the expansion velocity relative to orbital velocity (high-velocity winds will be loosely wound, expanding further in each orbital cycle). The overall normalization of $4\pi r^2\rho/|\dot{M}|$ for each model reflects the inverse of the wind expansion velocity—higher velocity winds have lower densities at the same mass loss rate. Spiral waves impart an approximately order of magnitude variation in local density in the orbital plane over the spherical mean. These fluctuations are quickly reduced out of the orbital plane—near the poles the density profile is a smooth r^{-2} pattern. We note that wind interaction regions lead to changes of wind angular velocity as angular momentum is redistributed and averaged among the interacting winds. However, because the velocity is primarily radial, these appear as only slight deviations in the streamlines in even the most extreme cases, as seen in the lower panel of Figure 1.4 for Model D.

4.2. Wind Acceleration and Velocity

This discussion of the interaction and superposition of the binary components' winds reveals the critical role of the winds' emergent velocity. Thermal winds accelerate due to radial pressure gradients from near rest through a critical point, at which the expansion velocity equals the sound of speed, eventually reaching supersonic radial expansion. In Figure 2, we analyze slices through the binary systems' orbital planes (figure set online shows each model). The upper panels show the Mach number in the corotating frame, and the lower panels show the Jacobi parameter. Velocity vectors are overplotted relative to the corotating frame. The Mach number and Jacobi parameter provide a window into the role that pressure gradients play in accelerating the wind away from the binary.

In the Mach number panels of Figure 2, we see the transition from subsonic outflow near the binary components to supersonic outflow with increasing radius—we mark the critical transition at $\mathcal{M}_{\rm rot} = 1$ with a contour. For spherical, isothermal winds, the critical point radius is $r_{\rm sonic} = GM/2c_s^2 = (\lambda/2)R_s$, where R_s is the radius of the stellar surface. This relation implies that we expect a larger subsonic outflow region for larger λ, because the shallower pressure gradients in these cases accelerate the wind more slowly. For some of the model parameter space, there are individual sonic transitions surrounding each binary component. This occurs for low λ, when the sonic radius becomes closer to the object radius, and for larger f_Φ, when the objects fill smaller fractions of their Roche lobes. However, other cases, such as Model G, in which $\lambda = 5$ and $f_\Phi = 2$, the sonic surface surrounds and encloses both binary components. For $\lambda = 2.5$, we observe that the sonic surface generally lies just outside of our surface boundary condition, is joined across both binary components only for the contact case of $f_\Phi = 1$. For $\lambda = 5$, when $f_\Phi \leqslant 2$ the sonic surface is joined, while for $\lambda = 10$, the sonic surface is joined across the binary components for all f_Φ studied. These findings are consistent with the simple estimate of joined sonic surfaces when $R_s/R_{\rm Roche} \gtrsim 2/\lambda$, or in terms of our model parameters, $f_\Phi \lesssim \lambda/2$.

The variation of the Jacobi parameter in model slices directly illustrates the role of pressure gradients in accelerating the wind. As we tabulate in Table 1, the surface Jacobi parameter, Equation (18), of the wind is equal to the effective potential of the surface. Ballistic, collisionless motion in the binary's gravity occurs at constant Jacobi parameter. By contrast, the increasing Jacobi parameter seen in the slices of Figure 2 is the result of the collisional nature of the fluid and the degree to which pressure gradients add kinetic energy to the flow. We mark the surface of zero Jacobi parameter in Figure 2, this represents the transition at which a collisionless particle is unbound relative to the binary system, ignoring the gas' internal energy. Under different model parameter variations, this $E_J = 0$ surface occurs at varying distances from the binary components. As for the sonic surface, at low λ and high f_Φ this transition separately surrounds the two binary components,

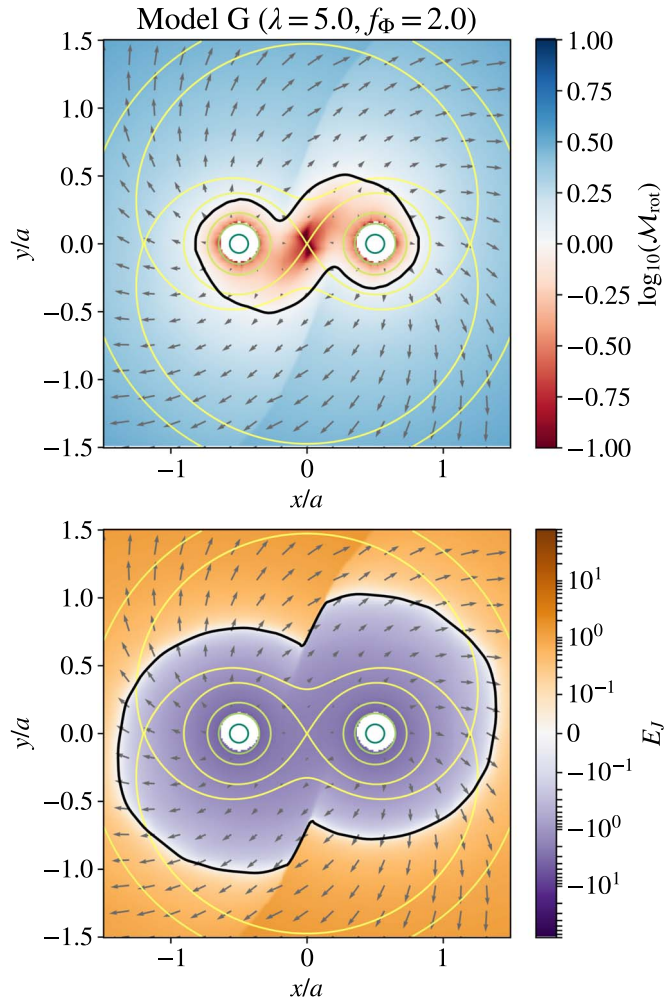

Figure 2. Slices of wind Mach number (upper panels) and Jacobi parameter (lower panels) at $z = 0$ in the corotating frame. The black contours shows the $\mathcal{M}_{\rm rot} = 1$ sonic surface and the $E_J = 0$ surface. The sonic transition occurs closest to the surfaces of the binary components for $\lambda = 2.5$ and furthest for $\lambda = 10$. The initial Jacobi parameter on the surface of the binary is $E_{J,0} = -2f_\Phi$. Because E_J is constant for collisionless motion in the binary potential, increases in E_J represent the acceleration of the wind by pressure gradients. The complete figure set (12 images) is available in the online journal and (MacLeod 2020).

(The complete figure set (12 images) is available.)

while for higher λ and lower f_Φ, this energetic transition surface surrounds the binary (for some of the parameter variations it occurs outside the $\pm 1.5a$ box of Figure 2).

The gradients of E_J are strongest for the highest sound speed winds, however, we note that outflowing streamlines trace increasing E_J in all cases. Streamlines along which Jacobi parameter is relatively constant, such as the circulating flow in the subsonic region close to the binary (in Model I, for example) indicate regions where circulation at constant energy is occurring mostly under the influence of the binary gravitational potential. By contrast with the increases observed in E_J, we note that the wind Bernoulli parameter, Equation (19), is observed to be constant within the winds to with approximately 2% of the surface Bernoulli parameter tabulated in Table 1. Together with our discussion of E_J, this indicates that the acceleration of the wind away from the binary is due to the energy associated with the gas enthalpy, h, which results in the increasing velocity of the wind along outflowing streamlines.

Figure 3 examines the development of radial velocity in the wind more quantitatively. Within a spherical volume of $r < 18a$, we sample each zone and plot its radial velocity, v_r, relative to r. The resulting velocity–radius phase plot is colored by relative mass per pixel. In each case we see that the wind is accelerated steeply over $r \lesssim 3a$ and then more gently as the wind continues to expand. A purely isothermal spherical wind will continue to grow in radial velocity over whatever scale the isothermal temperature is maintained. Our model winds with $\gamma = 1.01$ have finite, but large, asymptotic velocity. However, it is worth noting that the radial velocity is close to constant outside of the primary acceleration region that corresponds to the subsonic regions close to the binary in Figure 2. In Figure 3, we compare to the velocity profiles of corresponding spherical polytropic winds, following the formalism outlined in Appendix A. We solve the Bernoulli equation to model the wind with mass flux $\dot{M}$ equal to that of the binary simulation from an object with central mass M. These solutions are marked "Bernoulli wind" in Figure 3. We observe that the binary imparts some variation in the wind radial velocity at a given radius, but that the overall trend tracks that of the spherical wind, especially for $\lambda = 5$ and $\lambda = 2.5$. For $\lambda = 10$, we observe that the wind radial velocity in the binary simulations is larger than that predicted by the Bernoulli model.

Across binary parameters, we observe significant trends in the velocity to which the winds are accelerated. We measure the wind velocity at $r = 10a$ by taking the mass-weighted mean wind speed in a spherical shell $9.5 < r/a < 10.5$ and denote the result $v_{r,10}$. Beyond this, the velocity of our polytropic winds continues to expand slowly (and indeed an isothermal wind's velocity increases across as large a region as the isothermal temperature is maintained, see Parker 1958). Figure 4 shows the dependence of $v_{r,10}$ on the model parameters λ and f_Φ. We see that the highest velocity winds arise for high f_Φ and low λ. Because $c_{\rm s,s}^2 = -\Phi_{\rm s}/\lambda = -\Phi_{L_1} f_\Phi/\lambda$, clearly there is a trend that relates the wind velocity to the surface sound speed.

The lower panel of Figure 4 shows the resultant wind velocity as a function of the surface sound speed. These initial sound speeds are listed in Table 1. We note that the wind speed is well described by a power-law dependence,

$$\frac{v_{\rm r,10}}{v_{\rm orb}} \approx \frac{10}{3}\left(\frac{c_{\rm s,s}}{v_{\rm orb}}\right)^{4/3}, \tag{26}$$

which we additionally plot in Figure 4. Finally, we compare the trends in $v_{r,10}$ as a function of $c_{\rm s,s}$ by solving the Bernoulli equation for a spherical wind for each of the model parameters. The Bernoulli wind model accurately predicts the wind velocities for most of the simulations, except those with the lowest surface sound speeds. These models with low $c_{\rm s,s}$ exhibit higher radial velocities in the simulation, which appear to asymptote to $v_{r,10} \sim v_{\rm orb}$, implying that the binary's orbital motion plays a significant role in imparting radial velocity to these winds.

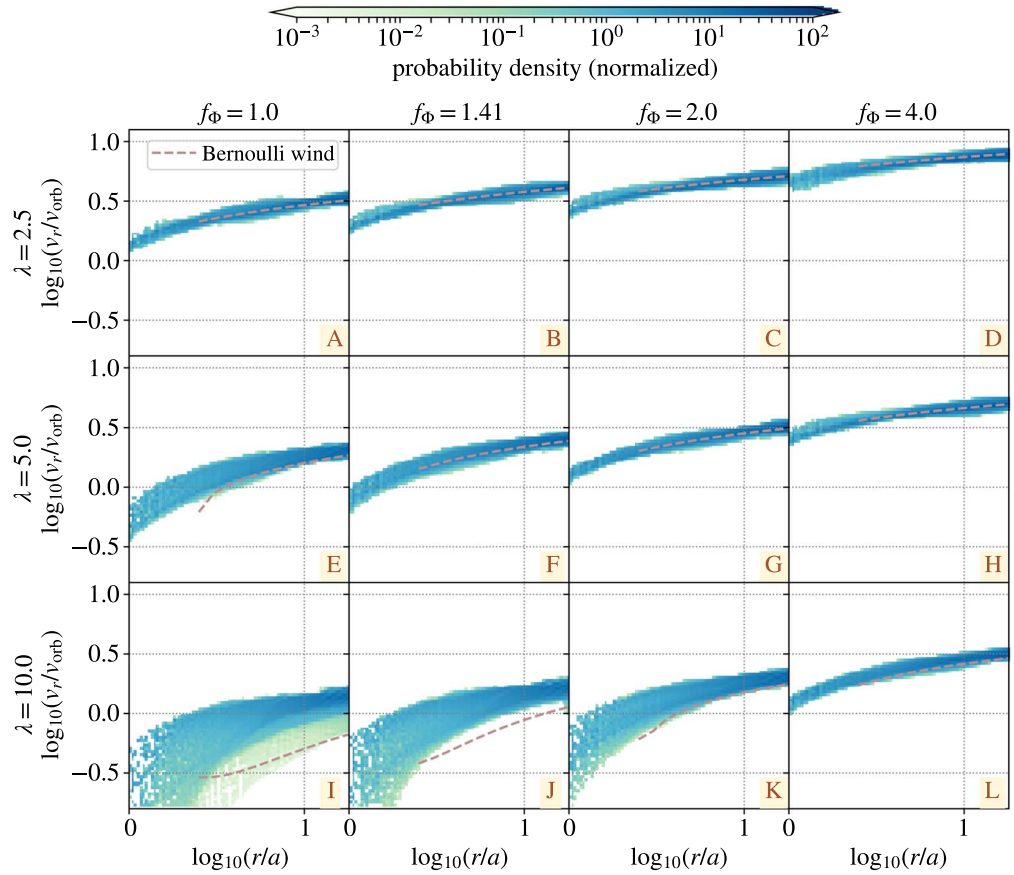

Figure 3. Radial velocity of wind with $r < 18a$ of the binary center of mass. The phase plot is colored by the normalized probability distribution function of wind mass in the r vs. v_r plane. In each case we compare to the velocity profile of polytropic winds from a single object with mass equal to the binary mass, and $\dot{M}$ equal to that of the binary simulation, labeled Bernoulli wind.

4.3. Mass Loss Rate

We measure the mass loss rate from the binary via the surface integral of Equation (7). The resulting mass loss rates are tabulated in Table 1. In all cases, mass is flowing away from the binary in a steady-state wind.

In Figure 5, we show the resulting mass loss rates as a function of wind velocity, labeling groups of f_Φ and λ model parameters (upper panel). At constant f_Φ, we observe that when the wind velocity (or surface sound speed) is larger (smaller λ), $|\dot{M}|$ increases. By contrast, when f_Φ increases at constant λ, the increased wind velocity implies decreasing $|\dot{M}|$, implying that the deeper potential well implied by larger f_Φ leads to more difficult escape for winds of a given velocity.

To some extent, these trends align with our analytic understanding of hydrodynamic winds. To establish a baseline for comparison, we define several estimates of the mass loss rate based on the binary parameters and surface sound speed, which are derived in Appendix B. We define:

(i) $\dot{M}_{\rm hi}$, twice the estimated isothermal mass loss rate from two individual objects of mass $M/2$, which have surface sound speed $c_{\rm s,s}$ and surface density $\rho_{\rm s}$. This estimate of the mass loss rate is derived by computing $2 \times 4\pi r_{\rm sonic}^2 \rho_{\rm sonic} c_{\rm s,s}$. As we will discuss, $\dot{M}_{\rm hi}$ applies in the regime of high-velocity winds that escape with little interaction with the binary potential.

(ii) $\dot{M}_{\rm lo}$, the outflow from the vicinity of the outer saddle points of the gravitational potential, L_2 and L_3, by estimating $2 \times \rho_{L_2} A_{L_2} v_{L_2}$, where $v_{L_2} \sim c_{\rm s,s}$, and the estimation of the other terms is discussed in detail in Appendix B. This estimate is applicable in the case of lower velocity winds that interact strongly with the binary potential.

We find that the following formula interpolates smoothly between the expected behaviors at high and low sound speed:

$$\dot{M}_{\rm est} \approx -\pi \left[\left(\frac{G^2 M^2}{2 c_{\rm s,s}^3} \right)^{-1} + \left(\frac{2 c_{\rm s,s}^3 a^3}{GM} \right)^{-1} \right]^{-1} \times \rho_{\rm s} \exp\left[-\lambda + \sqrt{\left(-\frac{\Phi_{L_2}}{c_{\rm s,s}^2} - \frac{1}{2} \right)^2 + \left(\frac{3}{2} \right)^2} \right]. \quad (27)$$

This estimating formula is plotted over the simulation data in Figure 5. This comparison shows that $\dot{M}_{\rm est}$ qualitatively captures the trends in $\dot{M}$ with binary parameters as well as the overall normalization of the mass loss rate.

In the lower panel of Figure 5, we compare the mass loss rates derived from the binary simulations to that estimated for two single objects, $\dot{M}_{\rm hi}$, as a function of wind velocity. This ratio expresses the enhancement in mass loss rate that results

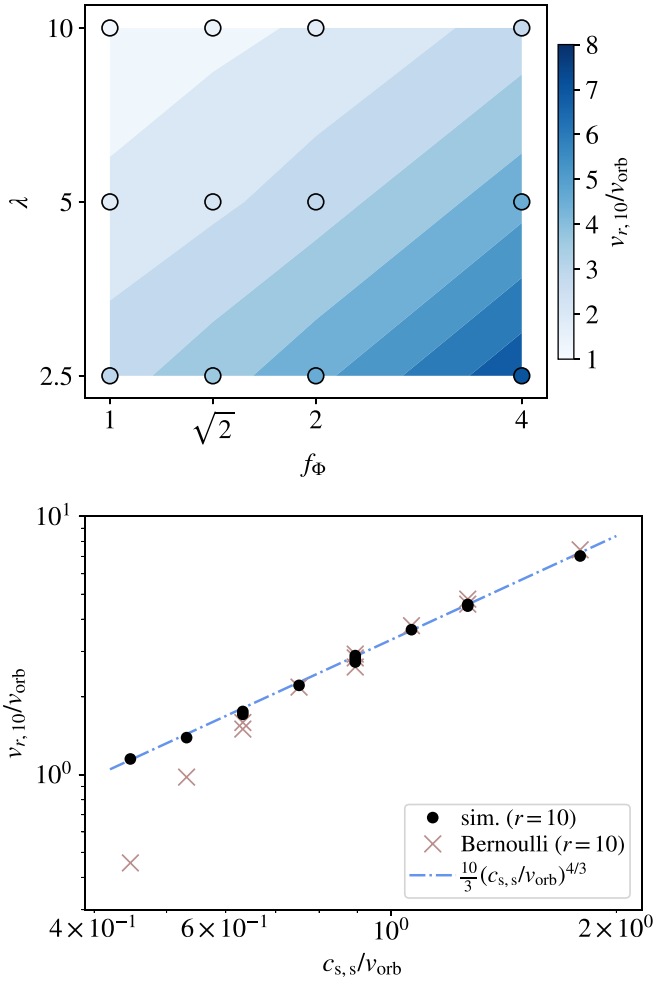

Figure 4. Wind radial velocity at $r = 10a$, normalized by the binary's orbital speed, $v_{\rm orb}$. The upper panel shows $v_{r,10}/v_{\rm orb}$ as a function of λ and f_Φ, while the lower panel shows that the dependence is primarily on the surface sound speed, $c_{\rm s,s}$. We compare to our solution of the Bernoulli equation for a spherical wind with mass flux $\dot{M}$ from an object of mass M, labeled Bernoulli wind. We observe that the spherical wind largely predicts the velocities at $10a$, except at lower $c_{\rm s,s}$, where there is some asymptotic behavior in the simulations with $v_{r,10} \sim v_{\rm orb}$, due to the orbital motion imparting radial velocity to the wind.

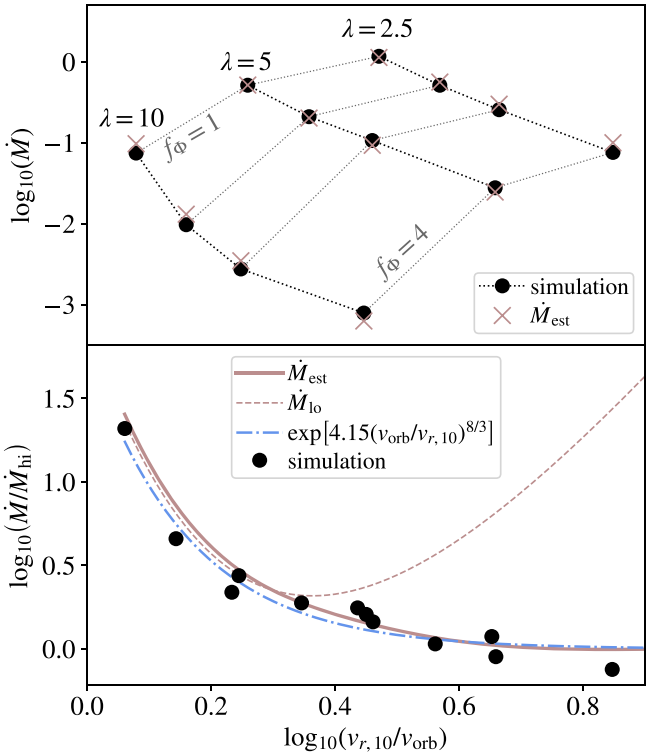

Figure 5. Mass loss rates from simulated twin-star binaries as a function of wind velocity, $v_{r,10}$ in units of $v_{\rm orb}$. In the upper panel, we show simulation $\dot{M}$ in code units compared to $\dot{M}_{\rm est}$, Equation (27). The highest mass loss rates occur for the combination of low λ and f_Φ. In the lower panel, we normalize $\dot{M}$ by $\dot{M}_{\rm hi}$, twice the expected single-object mass loss rate. At low wind velocities relative to the orbital velocity (equivalently for close binaries at fixed wind velocity), the mass loss rate from the binary is enhanced relative to the nonbinary equivalent.

from the binary potential at low wind velocities. Furthermore, we observe that the results collapse to a single velocity dependent relationship under this normalization. Through these comparisons, we observe that $\dot{M}_{\rm lo}$ captures the low-velocity behavior, but diverges at high velocity, while $\dot{M}_{\rm est}$ provides a reasonable approximation across the wind velocity range. The ratio of $\dot{M}_{\rm est}/\dot{M}_{\rm hi}$ is

$$\frac{\dot{M}_{\rm est}}{\dot{M}_{\rm hi}} \approx \frac{\exp\left[-\frac{3}{2}+\sqrt{\left(-\frac{\Phi_{L_2}}{c_{\rm s,s}^2}-\frac{1}{2}\right)^2+\left(\frac{3}{2}\right)^2}\right]}{1+\frac{1}{4}\left(\frac{v_{\rm orb}}{c_{\rm s,s}}\right)^6}, \quad (28)$$

which provides an analytic expression for the enhancement in the hydrodynamic wind from the binary solely as a function of its properties and surface sound speed.

Finally, the fact that the binary enhancement is a function of wind velocity indicates that we may be able to express the binary enhancement in wind mass loss rate as a function of the general property of wind velocity. Inspired by the functional form of Equation (28), we fit $\dot{M}/\dot{M}_{\rm hi}$ to an exponential function, and find that

$$\frac{\dot{M}}{\dot{M}_{\rm hi}} \approx \exp\left[2\left(\frac{-\Phi_{L_2}}{v_{r,10}^2}\right)^{4/3}\right], \approx \exp\left[4.15\left(\frac{v_{\rm orb}}{v_{r,10}}\right)^{8/3}\right] \quad (29)$$

provides a good description of the enhancement in $\dot{M}$ due to the fact that the objects are in a close binary. This function is shown with a dotted–dashed line in Figure 5. For example, for a pair of stars with fixed wind velocity, Equation (29) describes how the total mass loss rate changes as the binary separation (and thus $v_{\rm orb}$) changes.

One of the previously applied predictions for tidal enhancement of wind mass loss was postulated by Tout & Eggleton (1988, their Equation (2)). This model predicts an enhancement factor depending on the degree of Roche-lobe filling, according to

$$\frac{\dot{M}}{\dot{M}_{\rm hi}} = 1 + B_{\rm w}\left(\min\left[\frac{R}{R_{\rm L}}, \frac{1}{2}\right]\right)^6, \quad (30)$$

where $R/R_{\rm L}$ is the ratio of the stellar radius to the radius of the Roche lobe and $B_{\rm w}$ is a constant with nominal value 10^4. In Figure 6, we display the degree of wind enhancement as a

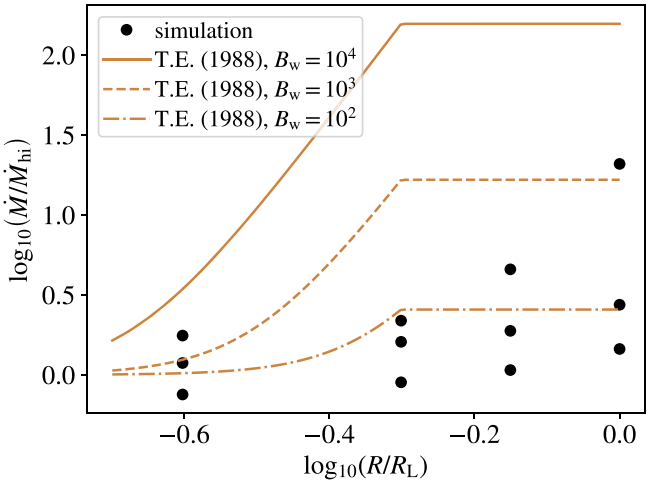

Figure 6. Comparison of simulated enhancement in mass loss rates compared to the single-object prediction, as a function of the ratio of the stellar radius to the Roche-lobe radius, $R/R_L = f_\Phi^{-1}$. The simulated values are compared to the prediction of Tout & Eggleton (1988), with three values of the constant B_w. Unlike the scaling with wind velocity shown in Figure 5, we find that the binary enhancement in wind mass loss is not single valued with degree of Roche-lobe occupancy, nor is its approximate magnitude described accurately by the Tout & Eggleton (1988) formula with the default value of $B_w = 10^4$.

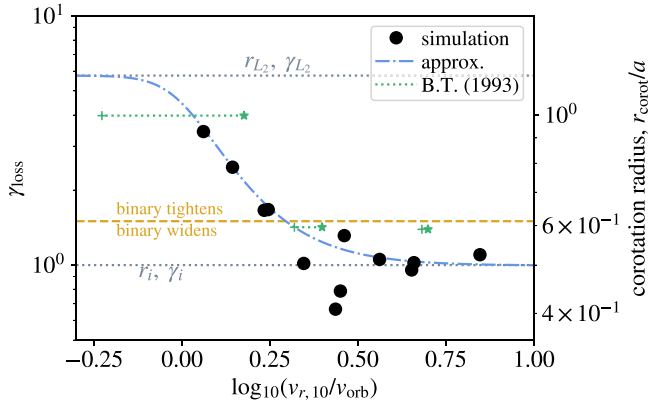

Figure 7. The dimensionless specific angular momentum carried by the wind, $\gamma_{loss} = l_{loss}/l_{bin}$, as a function of wind velocity, $v_{r,10}$. The right-hand axis expresses γ_{loss} in terms of the radius of corotation, $r_{corot}^2 = l_{loss}/\Omega = \gamma_{loss} l_{bin}/\Omega$, where Ω is the orbital frequency. A contour is plotted at the critical value of $\gamma_{loss} = 3/2$, which separates orbital evolution in which $\dot{a} > 0$ or $\dot{a} < 0$. High-velocity winds escape with $\gamma_{loss} \sim 1$. Slower velocity winds lead to $\gamma_{loss} > 1$ as the winds superimpose and interact with the binary effective potential. We compare to an approximating form, Equation (32), labeled "approx" and to the results of Brookshaw & Tavani (1993) for collisionless mass loss, labeled "B.T. (1993)."

function of Roche-lobe filling. By comparison to our simulation results, we see that the enhancement due to the presence of the binary is less than predicted by Tout & Eggleton (1988), and that our simulation results are multi-valued at a given degree of Roche-lobe filling. We therefore argue that wind velocity compared to orbital velocity, rather than Roche-lobe occupancy, is the most useful determinant of the rate of mass loss.

4.4. Angular Momentum Loss Rate

4.4.1. Simulated Loss Rates

We analyze angular momentum carried by the wind in terms of the surface integral of Equation (8). In this section, we refer to specific angular momenta in their dimensionless form, l/l_{bin}. Much like mass loss rates, we argue that important trends emerge as a function of wind velocity.

Figure 7 shows the dimensionless specific angular momentum of the wind, γ_{loss} and its dependence on wind velocity. We show an equivalent right-hand axis of the corotation radius implied by a given angular momentum,

$$r_{corot} = \sqrt{\frac{l_{loss}}{\Omega}}, \tag{31}$$

where l_{loss} is the angular momentum of the wind and Ω is the orbital frequency. Figure 7 demonstrates that angular momentum losses depend primarily on wind velocity:

(i) At high wind velocities, winds carry the angular momentum of the binary components, thus $\gamma_{loss} = \gamma_i = 1$ and $r_{corot} = r_i = a/2$. This high-velocity limit is a well-known case of an essentially noninteracting wind that freely escapes and is sometimes called "Jeans" mass loss.

(ii) In the opposite limit of low-velocity winds, material could be in corotation with the binary all the way out to the radius of the outer Lagrange point, $r_{L_2} \approx 1.2a$. This yields $\gamma_{L_2} = r_{L_2}^2 \Omega / l_{bin} \approx 5.76$. Given the shape of the effective potential outside of the outer Lagrange points, there is no mechanism (for a nonmagnetic wind) that would maintain corotation to larger radii. We therefore label this upper limit with r_{L_2}, γ_{L_2} in Figure 7.

In between these limits lies the critical value of $\gamma_{loss} = 3/2$ that separates orbital evolution in which the binary widens due to mass loss ($\gamma_{loss} < 3/2$) or tightens due to mass loss ($\gamma_{loss} > 3/2$).

Between the high and low-velocity limits of γ_{loss}, we must consider the effects of the extended surfaces of the binary components, hydrodynamic stresses from the superposition of winds, and the binary's gravitational torques on the outflowing material. That these overall processes reduce to a nearly one-dimensional function of wind velocity indicates that the primary physical effect must be the expansion velocity of the wind relative to the binary orbital velocity. Through studying our simulation snapshots, we observe that the wind is maintained in near-corotation out to approximately the sonic surface, along the simulation x-axis that connects the binary components. This is visualized most clearly in the snapshots of Figure 2. Thus, $r_{corot} \sim r_i + Gm_i/(2c_{s,s}^2) = r_i + GM/(4c_{s,s}^2)$ in the intermediate and high-velocity regimes, with a maximal limit at r_{L_2}.

Drawing on this functional form for inspiration, we develop the following approximating formula in terms of the more general property of wind velocity:

$$r_{corot} \approx \left[r_{L_2}^{-b} + \left(r_i^a + \left[\frac{GM}{v_{r,10}^2} \right]^a \right)^{-\frac{b}{a}} \right]^{-\frac{1}{b}}, \tag{32}$$

where the associated dimensionless specific angular momentum is

$$\gamma_{loss} \approx r_{corot}^2 \Omega / l_{bin}. \tag{33}$$

This expression provides a reasonable description of our simulation results across the various wind velocity regimes. We find that $a = 1.5$ and $b = 5$ fit the simulation data reasonably well. This curve is reproduced with a dotted–dashed line in Figure 7, where it is labeled "approx."

4.4.2. Comparison to Collisionless Mass Loss

In Figure 7 we compare our results for $\gamma_{\rm loss}$ to those derived by Brookshaw & Tavani (1993) under a fairly different set of model assumptions. Brookshaw & Tavani (1993) model a collisionless wind by integrating the ballistic trajectories of particles in the binary potential. This is conceptually similar to but more comprehensive in parameter coverage than earlier work by Lin (1977). The wind emerges from one component of the binary system, and Brookshaw & Tavani (1993) inject their wind with a radial velocity, which in their notation is written V and is normalized to the orbital velocity of the star losing mass. Thus, in our units the injection velocity is $v_{\rm in,BT} = V/2$ for $q = 1$. They denote the dimensionless specific angular momentum of particles in the wind as $h_{\rm cm}$, which can be converted to our notation (for $q = 1$) by $\gamma_{\rm loss} = 2h_{\rm cm}$. Finally, for comparison to our results measuring the wind velocity at $r = 10$, we compute what the ballistic wind velocity would be, assuming expansion from the single, wind-losing binary component

$$v_{10,\rm BT} \approx \sqrt{v_{\rm in,BT}^2 - 2GM_*\left(\frac{1}{R_*} - \frac{1}{r}\right)} \approx \sqrt{v_{\rm in,BT}^2 - 1.9}\,, \quad (34)$$

where the numerical result comes from $r = 10$, $GM_* = 0.5$, and $R_* = 0.5$. Because neither of these velocities is completely comparable to those in our hydrodynamic simulations (the velocity profile of decelerating ballistic particles is quite different from that of our accelerating wind), we show both $v_{\rm in,BT}$ with stars, and $v_{10,\rm BT}$ with plus symbols in Figure 7.

Despite the differences in model, we observe a largely similar trend in the results of Brookshaw & Tavani (1993) and our hydrodynamic simulations. For $v_{r,10} < 2$, we find $\gamma_{\rm loss} > 1$, while for $v_{r,10} \gtrsim 2$, $\gamma_{\rm loss}$ asymptotes (in the case of Brookshaw & Tavani 1993 to $\gamma_{\rm loss} \approx 1.39$ versus $\gamma_{\rm loss} \approx 1$ in our simulations). The physical origin of these similar results is somewhat different. In the case of Brookshaw & Tavani (1993), the particles acquire angular momentum (beyond that with which they are injected) through gravitational stresses alone, while in our simulations, hydrodynamic stresses play a role in imparting angular momentum to escaping wind. Brookshaw & Tavani (1993) do note, however, that in the cases of low-velocity wind only the particles injected on the outer edges of the binary are lost. In our simulations, pressure gradients play a similar regulatory role in allowing material to circulate toward the outer Lagrange points L_2 and L_3 before it is carried away.

4.4.3. Origin of Angular Momentum in Interacting Winds

In Figure 8, we decompose $\gamma_{\rm loss}$ into the contributing components resulting from gravitational stress ($\gamma_{\rm grav}$) or from hydrodynamic stress ($\gamma_{\rm wind}$), Equations (15) and (17), respectively. This decomposition allows us to trace the origin of angular momentum acquired by the wind as it flows away from the binary. Hydrodynamic stresses include surface forces from the imposition of constant pressure and density along the equipotential surface defined by f_Φ, Equation (6), and the subsequent collisional nature of the gas as it expands away from the binary components and the two, initial separate, winds superimpose. Gravitational stresses arise from net torques on the wind from the binary's gravity and the resulting exchange between wind and orbital angular momentum. For example, leading edge overdensities in the flow torque the binary forward in its orbit, while trailing overdensities torque the binary backward.

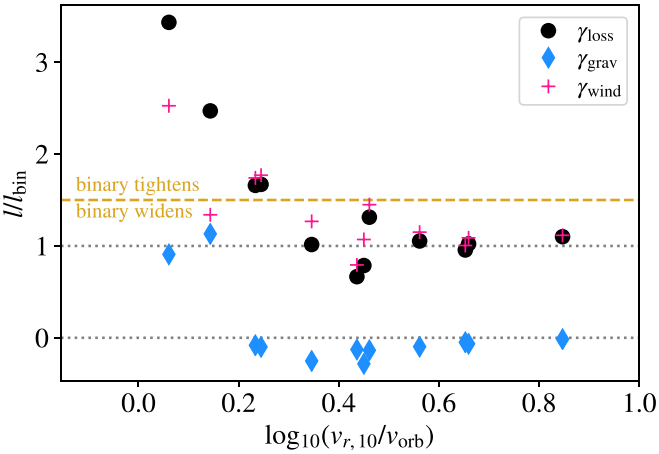

Figure 8. Dimensionless angular momenta of the wind resulting from hydrodynamic stresses ($\gamma_{\rm wind}$) or gravitational stresses ($\gamma_{\rm grav}$). Together these components comprise the total dimensionless angular momentum, $\gamma_{\rm loss}$. All plotted in terms of wind velocity, approximated by $v_{r,10}$. We find that $\gamma_{\rm wind} > 0$ in all cases, and is largest for low f_Φ and high λ, which lead to low wind velocities. The gravitational addition to l can be either positive or negative, but has smaller magnitude that $\gamma_{\rm wind}$.

Figure 8 reveals that $\gamma_{\rm wind}$ is always greater than zero. It is near unity at high wind velocities, where winds establish separately around each binary component before superimposing. At lower wind velocities, $\gamma_{\rm wind}$ takes on values significantly larger than unity, driving the bulk of the increase in $\gamma_{\rm loss}$ that we have noted with decreasing velocity in Figure 7. The expanded subsonic region surrounding the pairs at lower wind velocities contributes to an extended region in which pressure forces act to redistribute flow away from the overconcentration near the binary center of mass, imparting it with additional angular momentum. The extended surface area of the binary components at lower f_Φ also contributes to this addition of angular momentum in the these cases, as the wind can be seen to "slide" off of the leading edges of the orbiting stars.

Gravitational stresses as measured by $\gamma_{\rm grav}$ in Figure 8 approach zero at high wind velocities—the wind is essentially spherical and noninteracting. At intermediate velocities $\gamma_{\rm grav}$ is negative, implying that gravitational stresses remove angular momentum from the wind, adding it to the binary. At low velocities, $\gamma_{\rm grav} > 0$, and the binary potential imparts angular momentum to the slowly expanding wind. At intermediate wind velocities, $2.5 < v_{r,10}/v_{\rm orb} < 3$, we observe the widest range of $\gamma_{\rm loss}$ at similar velocity values. The decomposition by component is useful in disentangling this feature. The highest value of $\gamma_{\rm loss}$ in this regime comes from Model A, for which $f_\Phi = 1$. The Roche-lobe filling surfaces of this binary contributes to a high $\gamma_{\rm wind}$, which is slightly reduced by the negative $\gamma_{\rm grav}$. The lowest value in this range comes from Model L, with $f_\Phi = 4$. Here $\gamma_{\rm wind} = 0.79$, but the eventual value of $\gamma_{\rm loss}$ is significantly lower, $\gamma_{\rm loss} = 0.67$ due to the negative contribution of $\gamma_{\rm grav}$. A similar circumstance occurs with Model G, in which $\gamma_{\rm wind} > 1$ but $\gamma_{\rm loss} < 1$ due to a negative $\gamma_{\rm grav}$. Thus, while the high-velocity asymptote of the wind specific angular momentum is $\gamma_{\rm loss} \to 1$, in the intermediate wind velocity regime, there appears to be some variation at fixed wind velocity depending on other binary parameters, and values of $\gamma_{\rm loss} < 1$ are possible in this regime.

5. Discussion

5.1. Limitations and Astrophysical Applicability

We have studied a highly idealized numerical problem, in which, among other assumptions, a perfectly symmetric pair of stars, synchronously rotating with their orbit, develop equal winds from high-temperature surfaces. We adopt a nearly isothermal equation of state for the wind thermodynamics. The resulting hydrodynamic winds accelerate through a sonic point as they expand away from the binary. This model is an extension of one of the simplest models of the solar wind, the Parker (1958) wind model, though the details are slightly different for $\gamma = 1.01$, as described in Appendix A.

Depending on stellar surface properties, one of several different wind-acceleration mechanisms is more likely to contribute to the phases when stars lose the most mass. In low-temperature stellar surfaces, radiation pressure on dust that forms within the cooling and expanding wind is a significant wind driving mechanism. Because the radiative flux scales with r^{-2}, in its simplest form this sort of wind driving mechanism has the effect of reducing the gravitational attraction of the stars by a factor (which in general is not spatially constant because the formation of dust highly effects the opacity and thus the Eddington ratio as a function of radius). In higher-temperature stellar surfaces, the primary wind driving mechanism is radiation coupling to Doppler-broadened metal absorption lines. A similarity is that these massive stars can have luminosities approaching the Eddington luminosity for electron scattering, and thus have reduced effective gravity as well. In the case of a line-driven wind, the resulting wind-acceleration profile differs somewhat from that of a hydrodynamic or dust-driven wind (Lamers & Cassinelli 1999).

What each wind model shares is the acceleration of wind from near rest at the stellar surface to some asymptotic velocity at large radii. When the binary system has separation comparable to the characteristic radius of acceleration, interaction with the binary potential is especially important (e.g., Chen et al. 2017; El Mellah et al. 2020). In the case of multiple, radiation driven winds, the superposition of radiative forces and the winds themselves are also important (Canto et al. 1996; Pittard 2009; Lamberts et al. 2012; Pittard & Dawson 2018). Future work could expand on the simplest-case scenario that we have adopted in this paper to explore how significant these various wind-acceleration mechanisms are in determining the morphology of angular momentum carried by the wind from twin-star binaries.

Although a final conclusion awaits these further studies, we hypothesize that the velocity–mass-loss and velocity–angular-momentum connections established in Figures 5 and 7 will be relatively robust regardless of the particulars of the wind-acceleration process, given that they can be expressed in terms of the relatively general property of wind velocity. At a minimum, these models are likely more appropriate than assuming that the fast-wind approximation of unmodified mass loss rate at $\gamma_{\rm loss} \sim 1$ holds regardless of binary properties. Finally, we note that Equations (29) and (32) provide convenient approximations of our simulation results that can be applied on the basis of the ratio of the wind velocity to the orbital velocity, a property that is simple to estimate in binary population models to aid the application of our simulation results to real systems.

5.2. Orbital Evolution of Close Twin Binaries

To illustrate the implications of our findings for close twin binaries, we compute the orbital evolution of a stellar pair of

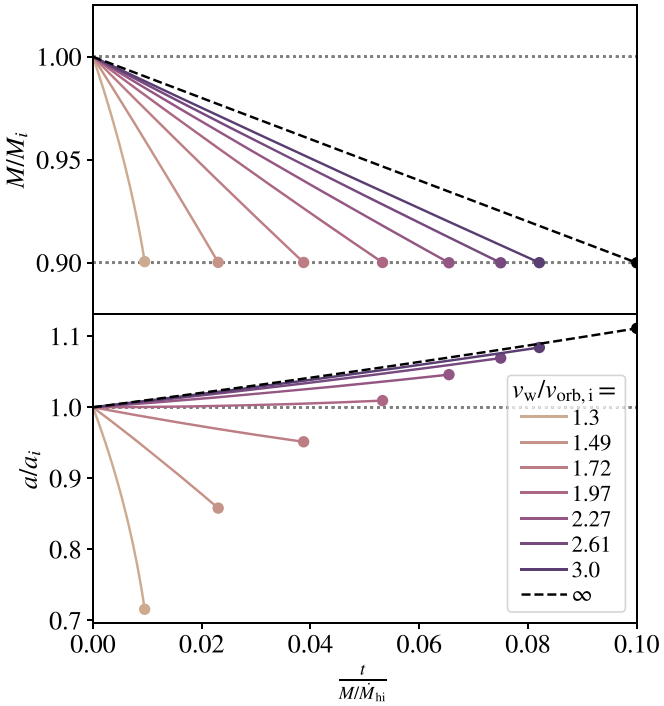

Figure 9. Binary mass and separation as a function of time, given different initial ratios of wind velocity to orbital velocity. In each case we consider the range of times during which mass decreases to 90% of its original value. For lower wind velocities, the mass loss rate is enhanced and the orbit tightens in response.

mass M and separation a, with initial mass M_i and separation a_i. We assume a constant wind speed, $v_{\rm w}$, and we associate this wind speed with our measured wind speeds at $r = 10a$, $v_{r,10}$. We then apply the approximating forms of Equations (29) and (32) to compute the resulting orbital evolution as a function of $\gamma_{\rm loss}$, following Equation (23). The result is shown in Figure 9. Binaries with high-velocity winds expand, as expected with Jeans mass loss of high-velocity winds. Binaries with lower velocity winds lose mass more rapidly and also contract, in the most extreme cases quite severely.

A key application of these results may be to the chemically homogeneous evolutionary model for the formation of merging binary black holes (de Mink & Mandel 2016; Mandel & de Mink 2016; Marchant et al. 2016; Song et al. 2016). In this model, a near-contact massive binary evolves under the influence of tidal stresses to acquire additional rotational mixing such that all or nearly all of each star eventually collapses to a black hole (de Mink et al. 2009). One such massive contact binary has been observed in 30 Doradus, VFTS352, which is a near-twin binary with total mass of approximately $59 M_\odot$ (Almeida et al. 2015). In many cases, the resulting black hole pairs are close enough to merge in less than the age of the universe (for one example, see Figure 4 of Marchant et al. 2016).

Throughout their evolution, binaries undergoing chemically homogeneous evolution lose a portion of their mass to winds. To give a specific example, the exemplary system evolved in Figure 2 of Marchant et al. (2016) loses 10% of its mass on the main sequence and 20% prior to the collapse at metallicity of $Z_\odot/50$. Because winds are largely metal-line driven, this fraction is thought to be metallicity dependent (e.g., Puls et al. 2008). The impact of this wind mass loss on the binary orbits may have important implications for the separation of the

binary system. If the separation widens too far, a pair might separate far enough that their remnant black holes would not merge under the influence of gravitational radiation. On the other hand, if the separation tightens too dramatically, a pair of stars might merge and produce a single, more massive black hole remnant.

Mandel & de Mink (2016) and de Mink & Mandel (2016) consider a number of variations of the wind mass loss model, and demonstrate that this is a central parameter in determining the number of merging systems that are observable by LIGO. In one of their model variations, winds are assumed to carry the angular momentum predicted by the model of Brookshaw & Tavani (1993). The assumption of $\gamma_{\rm loss} > 1$ yields their highest predicted observable merger rates at LIGO design sensitivity (see Table 1 of de Mink & Mandel 2016). In a simple sense, this is because any changes in binary separation are amplified by the gravitational-wave merger time that scales as a^4. By contrast, most population models, such as BSE (Hurley et al. 2002), the chemically homogenous models of Marchant et al. (2016), MOBSE (Giacobbo et al. 2018), and SEVN (Spera et al. 2019), currently adopt the fast-wind approximation of $\gamma_{\rm loss} = 1$ for lack of a complete and more sophisticated prescription.

Our results suggest that the relative magnitude of the wind speed to the orbital velocity may be a simple representative parameter that determines the binary enhancement in mass loss rate as well as the angular momentum carried away from the binary with the wind (see also Brookshaw & Tavani 1993; Jahanara et al. 2005; Chen et al. 2017, 2018). Population models incorporating these approximations may be useful step toward understanding how initial properties of close binaries map through their main sequence evolution and toward the formation of binary black holes that may eventually merge. Indeed, the similarity between our model results and those of Brookshaw & Tavani (1993) are suggestive of the high predicted black hole merger rates observable by the LIGO-Virgo network ($1200\,{\rm yr}^{-1}$ detections at design sensitivity) under this model variation of Mandel & de Mink (2016) and de Mink & Mandel (2016).

6. Summary and Conclusion

We have created and analyzed models of thermal winds from twin-star close binaries in circular orbits. Each of our models adopts $q = 1$, and we set the binary components surface based on a factor times the potential at the L_1 Lagrange point, f_Φ. The wind initial sound speed is set based on a hydrodynamic escape parameter, λ. We examine the emergent wind distributions in each model, as well as the fluxes of mass and angular momentum carried away from the binary by the wind.

Some key findings of our study are:

1. The acceleration of winds from about the binary components leads to a symmetric outflow traced by spiral density waves in the plane of the orbit (Figure 1). The subsonic acceleration region can surround either the individual binary components, or the entire binary, when $f_\Phi \lesssim \lambda/2$ (Figure 2). The resulting outflow is largely similar to that of a spherical wind, with the addition of density and velocity waves in the equatorial plane due to the binary's motion (Figure 1).
2. Eventual wind radial velocities are related to the surface sound speeds. At low sound speeds, radial velocities exceed that of a single-object wind model, implying that orbital motion imparts additional kinetic energy to the wind (Figures 3 and 4).
3. Mass loss rates from the binary are enhanced relative to the estimated superposition of two single-object winds. This effect is best modeled as a function of wind velocity, as shown in Figure 5, and approximated by Equation (29).
4. The specific angular momentum carried by the wind depends primarily on the wind velocity as well (Figure 7). It is enhanced well beyond the binary's specific angular momentum for the slower winds, which circulate around the binary before escaping near the outer Lagrange points (Figure 8), and we provide an approximating formula in Equation (32).

The dependence of wind mass loss rate and specific angular momentum on wind velocity, as modeled by Equations (29) and (32) may have implications for models of massive, near-contact twin binaries undergoing chemically homogeneous evolution due to rotationally enhanced mixing. In particular, Mandel & de Mink (2016) and de Mink & Mandel (2016) argue that the model is sensitive to both the mass and angular momentum carried by winds. Our results suggest that for contact systems with low-velocity winds, mass loss rates and angular momentum loss rates will both be enhanced. Comparison to the model variations of Mandel & de Mink (2016) and de Mink & Mandel (2016) suggest that the high angular momentum loss rates may indicate an enhancement in the portion of binaries that undergo chemically homogeneous evolution that leave binary black hole remnants that can merge in a Hubble time. Productive avenues for future study include modeling twin-star winds that are radiatively, rather than thermally, accelerated, and applying findings of mass and angular momentum loss rates in population studies of detectable binary black hole mergers with the LIGO-Virgo network.

Software and data to reproduce the results in this paper are made public in parallel to this publication via the Zenodo data set(doi:10.5281/zenodo.3939284) and associated software repository hosted on github[3] and Zenodo (MacLeod 2020).

M.M. is grateful to A. Oklopčić for many discussions on hydrodynamic winds, and to I. Mandel and S. de Mink for conversations about massive, contact binaries that together inspired this work. This work was supported by the National Science Foundation under Grant No. 1909203. Resources supporting this work were provided by the NASA High-End Computing (HEC) Program through the NASA Advanced Supercomputing (NAS) Division at Ames Research Center. This work used the Extreme Science and Engineering Discovery Environment (XSEDE), which is supported by National Science Foundation Grant No. ACI-1548562. In particular, use of XSEDE resource Stampede2 at TACC through allocation TG-AST190046 enabled this work.

Software: IPython (Pérez & Granger 2007); SciPy (Virtanen et al. 2020); NumPy (van der Walt et al. 2011); matplotlib (Hunter 2007); Astropy (Astropy Collaboration et al. 2013); Athena++ (Stone et al. 2020); XSEDE (Towns et al. 2014); TwinWinds (MacLeod 2020).

[3] https://github.com/morganemacleod/TwinWinds

Appendix A
Spherical Polytropic Winds

Spherically symmetric polytropic winds serve as a useful benchmark against which to compare the binary wind. We consider a wind that satisfies the mass continuity equation

$$\dot{M} = 4\pi r^2 \rho v, \tag{A1}$$

and has a polytropic equation of state

$$P = K\rho^{\gamma}. \tag{A2}$$

The Bernoulli parameter is preserved along a streamline

$$\mathcal{B} = \frac{v^2}{2} - \frac{GM}{r} + \frac{\gamma}{\gamma - 1}\frac{P}{\rho}, \tag{A3}$$

where the potential is $-GM/r$. From the surface condition at the launching of the wind, we can solve for $K = P_s/\rho_s^{\gamma}$. Solving the continuity equation for ρ, we can rewrite the Bernoulli equation as

$$\mathcal{B} = \frac{v^2}{2} - \frac{GM}{r} + \frac{\gamma}{\gamma - 1}K\left(\frac{\dot{M}}{4\pi r^2 v}\right)^{\gamma - 1}, \tag{A4}$$

with known initial conditions, the constants B, K are known. If we select a value for $\dot{M}$, we can numerically solve for the full solution for the velocity profile $v(r)$.

Appendix B
Estimates of Mass Loss Rate

B.1. Single-object Regime

We begin with the derivation of the wind mass loss rate from a single object of mass m. We assume an isothermal wind, which is similar to, but not identical to, the $\gamma_{ad} = 1.01$ model applied in our hydrodynamic simulations. In this case, we use the sonic point, at which the wind radial Mach number is unity, to anchor our solution. Thus, $\dot{m} \approx -\pi r_{sonic}^2 \rho_{sonic} v_{sonic}$. The velocity is equal to the isothermal sound speed, $v_{sonic} = c_s$ of the isothermal gas. We can estimate the sonic radius as

$$r_{sonic} = \frac{Gm}{2c_s^2}. \tag{B1}$$

Then, we need to estimate the density at the sonic point. In the subsonic, quasi-hydrostatic region, the density follows exponential decay, so we use that solution to relate the sonic-point density to the surface density as

$$\rho_{sonic} = \rho_s \exp\left(\frac{\Phi_s}{c_s^2} - \frac{\Phi_c}{c_s^2} - \frac{1}{2}\right). \tag{B2}$$

The first two terms in the exponential express the potential difference between the surface (Φ_s) and the sonic point (Φ_s), dividing by the sound speed squared yields the number of scale heights in the quasi-hydrostatic solution. The $\exp(-1/2)$ factor comes from solving the Bernoulli equation for the nonzero velocities in the subsonic region and accounts for the lower density realized with $v_{sonic} = c_s$ (page 68 Lamers & Cassinelli 1999). We note that $\Phi_s/c_s^2 = -\lambda$, and following Equation (B1), $-\Phi_c/c_s^2 = 2$. Thus, the expression above can be simplified to

$$\rho_{sonic} = \rho_s \exp\left(\frac{3}{2} - \lambda\right). \tag{B3}$$

Thus, the estimated mass loss rate is

$$\dot{m} \approx -\pi\frac{(Gm)^2}{c_s^3}\rho_s \exp\left(\frac{3}{2} - \lambda\right). \tag{B4}$$

B.2. Binary Regime

Here we estimate a mass loss rate from an equal-mass binary of mass M, assuming that a subsonic region encloses the binary components (thus, wind escapes from the binary, rather than single components). Under these conditions, we need to take into account the binaries effective potential, including the gravity of the two components and the rotating frame in which the wind is launched. This implies that the wind's subsonic quasi-hydrostatic region cannot expand beyond the outer saddle points of the effective potential, L_2 and L_3. We will, therefore, derive a mass loss rate considering the flow through these outer Lagrange points as $\dot{M} \approx A_{L_2}\rho_{L_2}v_{L_2}$. Much like flow through the L_1 Lagrange point, we assume that material has a velocity equal to its sound speed as it crosses the saddle point, thus, $v_{L_2} = c_s$ (Lubow & Shu 1975; Jackson et al. 2017). The area at the outer Lagrange point is estimated by similar analogy to work considering the L_1 Lagrange point. The degree to which gas can spread from the precise saddle point is determined by the scale height, thus, to order of magnitude,

$$A_{L_2} \sim \frac{\pi c_s^2}{\Omega^2}, \tag{B5}$$

where $\Omega^2 = GM/a^3$ is the binary orbital frequency.

The density at the outer Lagrange point is estimated by analogy to the single-object case, as

$$\rho_{L_2} = \rho_s \exp\left(\frac{\Phi_s}{c_s^2} - \frac{\Phi_{L_2}}{c_s^2} - \frac{1}{2}\right), \tag{B6}$$

$$= \rho_s \exp\left(-\lambda - \frac{\Phi_{L_2}}{c_s^2} - \frac{1}{2}\right), \tag{B7}$$

where Φ_{L_2} is the effective potential evaluated at the outer Lagrange point. For an equal-mass binary, $\Phi_{L_2} \approx 0.86424\Phi_{L_1} = -1.72848GM/a$.

Combining these terms yields

$$\dot{M} \approx -2\frac{\pi c_s^3}{\Omega^2}\rho_s \exp\left(-\lambda - \frac{\Phi_{L_2}}{c_s^2} - \frac{1}{2}\right), \tag{B8}$$

$$\approx -2\frac{\pi c_s^3 a^3}{GM}\rho_s \exp\left(-\lambda - \frac{\Phi_{L_2}}{c_s^2} - \frac{1}{2}\right), \tag{B9}$$

where the additional factor of 2 accounts for symmetric loss through two equal outer Lagrange points. This derivation could be generalized to an unequal binary by providing separate estimates of ρ_{L_2} and ρ_{L_3}.

B.3. Application to Simulation Models

To apply these estimates to our simulation models, we begin by acknowledging that our simulation is not strictly isothermal. For the purpose of comparison, however, we associate the

surface sound speed, $c_{s,s}$, with the isothermal sound speed of the previous subsections.

Next, we identify the single-object regime as applicable when winds are sufficiently high velocity as to be relatively unaffected by the binary's orbital motion and potential. In this regime, $r_{\rm sonic} \ll a$ (or similarly $c_{s,s} \gg v_{\rm orb}$), and the wind escapes from an effectively single object prior to interacting with the binary. The binary regime applies under opposite conditions, when $r_{\rm sonic} \gtrsim a$ (or $c_{s,s} \lesssim v_{\rm orb}$). In the effectively single regime, we need to account for mass loss from two objects, each of mass $m = M/2$. With these associations, we define

$$\dot{M}_{\rm hi} \approx -\frac{\pi}{2}\frac{(GM)^2}{c_s^3}\rho_s \exp\left(\frac{3}{2} - \lambda\right), \tag{B10}$$

which approximates the binary mass loss rate in the high wind-velocity regime, and

$$\dot{M}_{\rm lo} \approx -2\frac{\pi c_s^3 a^3}{GM}\rho_s \exp\left(-\lambda - \frac{\Phi_{L_2}}{c_s^2} - \frac{1}{2}\right), \tag{B11}$$

which approximates the binary mass-loss rate in the low wind-velocity regime.

ORCID iDs

Morgan MacLeod https://orcid.org/0000-0002-1417-8024
Abraham Loeb https://orcid.org/0000-0003-4330-287X

References

Almeida, L. A., Sana, H., de Mink, S. E., et al. 2015, ApJ, 812, 102
Astropy Collaboration, Robitaille, T. P., Tollerud, E. J., et al. 2013, A&A, 558, A33
Bermúdez-Bustamante, L. C., García-Segura, G., Steffen, W., & Sabin, L. 2020, MNRAS, 493, 2606
Blondin, J. M. 1994, ApJ, 435, 756
Blondin, J. M., Kallman, T. R., Fryxell, B. A., & Taam, R. E. 1990, ApJ, 356, 591
Blondin, J. M., Stevens, I. R., & Kallman, T. R. 1991, ApJ, 371, 684
Blondin, J. M., & Woo, J. W. 1995, ApJ, 445, 889
Bosch-Ramon, V., Barkov, M. V., Khangulyan, D., & Perucho, M. 2012, A&A, 544, A59
Brookshaw, L., & Tavani, M. 1993, ApJ, 410, 719
Canto, J., Raga, A. C., & Wilkin, F. P. 1996, ApJ, 469, 729
Čechura, J., & Hadrava, P. 2015, A&A, 575, A5
Chen, Z., Blackman, E. G., Nordhaus, J., Frank, A., & Carroll-Nellenback, J. 2018, MNRAS, 473, 747
Chen, Z., Frank, A., Blackman, E. G., Nordhaus, J., & Carroll-Nellenback, J. 2017, MNRAS, 468, 4465
de Mink, S. E., Cantiello, M., Langer, N., et al. 2009, A&A, 497, 243
de Mink, S. E., & Mandel, I. 2016, MNRAS, 460, 3545
de Mink, S. E., Sana, H., Langer, N., Izzard, R. G., & Schneider, F. R. N. 2014, ApJ, 782, 7
de Val-Borro, M., Karovska, M., & Sasselov, D. 2009, ApJ, 700, 1148
de Val-Borro, M., Karovska, M., Sasselov, D. D., & Stone, J. M. 2017, MNRAS, 468, 3408
Duchêne, G., & Kraus, A. 2013, ARA&A, 51, 269
El Mellah, I., Bolte, J., Decin, L., Homan, W., & Keppens, R. 2020, A&A, 637, A91
El Mellah, I., Sander, A. A. C., Sundqvist, J. O., & Keppens, R. 2019, A&A, 622, A189
El Mellah, I., Sundqvist, J. O., & Keppens, R. 2018, MNRAS, 475, 3240
Giacobbo, N., Mapelli, M., & Spera, M. 2018, MNRAS, 474, 2959
Huarte-Espinosa, M., Carroll-Nellenback, J., Nordhaus, J., Frank, A., & Blackman, E. G. 2013, MNRAS, 433, 295
Hunter, J. D. 2007, CSE, 9, 90
Hurley, J. R., Tout, C. A., & Pols, O. R. 2002, MNRAS, 329, 897
Jackson, B., Arras, P., Penev, K., Peacock, S., & Marchant, P. 2017, ApJ, 835, 145
Jahanara, B., Mitsumoto, M., Oka, K., et al. 2005, A&A, 441, 589
Lamberts, A., Dubus, G., Lesur, G., & Fromang, S. 2012, A&A, 546, A60
Lamberts, A., Fromang, S., & Dubus, G. 2011, MNRAS, 418, 2618
Lamberts, A., Fromang, S., Dubus, G., & Teyssier, R. 2013, A&A, 560, A79
Lamers, H. J. G. L. M., & Cassinelli, J. P. 1999, Introduction to Stellar Winds (Cambridge: Cambridge Univ. Press)
Lemaster, M. N., Stone, J. M., & Gardiner, T. A. 2007, ApJ, 662, 582
Lin, D. N. C. 1977, MNRAS, 179, 265
Lubow, S. H., & Shu, F. H. 1975, ApJ, 198, 383
MacLeod, M. 2020, Morganemacleod/TwinWinds: v1.0, Zenodo, doi:10.5281/zenodo.4000203
Mandel, I., & de Mink, S. E. 2016, MNRAS, 458, 2634
Marchant, P., Langer, N., Podsiadlowski, P., Tauris, T. M., & Moriya, T. J. 2016, A&A, 588, A50
Mohamed, S., & Podsiadlowski, P. 2007, in ASP Conf. Ser. 372, 15th European Workshop on White Dwarfs, ed. R. Napiwotzki & M. R. Burleigh (San Francisco, CA: ASP), 397
Murray, C. D., & Dermott, S. F. 1999, Solar System Dynamics (Cambridge: Cambridge Univ. Press)
Nagae, T., Oka, K., Matsuda, T., et al. 2004, A&A, 419, 335
Owocki, S. P., & Gayley, K. G. 1995, ApJL, 454, L145
Parker, E. N. 1958, ApJ, 128, 664
Parkin, E. R., & Gosset, E. 2011, A&A, 530, A119
Parkin, E. R., & Pittard, J. M. 2008, MNRAS, 388, 1047
Parkin, E. R., Pittard, J. M., Corcoran, M. F., & Hamaguchi, K. 2011, ApJ, 726, 105
Parkin, E. R., Pittard, J. M., Nazé, Y., & Blomme, R. 2014, A&A, 570, A10
Pérez, F., & Granger, B. E. 2007, CSE, 9, 21
Pittard, J. M. 1998, MNRAS, 300, 479
Pittard, J. M. 2007, ApJL, 660, L141
Pittard, J. M. 2009, MNRAS, 396, 1743
Pittard, J. M., & Dawson, B. 2018, MNRAS, 477, 5640
Puls, J., Vink, J. S., & Najarro, F. 2008, A&ARv, 16, 209
Saladino, M. I., & Pols, O. R. 2019, A&A, 629, A103
Sana, H., de Mink, S. E., de Koter, A., et al. 2012, Sci, 337, 444
Savonije, J. 1983, in Accretion-Driven Stellar X-ray Sources, ed. W. H. G. Lewin & E. P. J. van den Heuvel (Cambridge: Cambridge Univ. Press), 343
Song, H. F., Meynet, G., Maeder, A., Ekström, S., & Eggenberger, P. 2016, A&A, 585, A120
Spera, M., Mapelli, M., & Bressan, A. 2015, MNRAS, 451, 4086
Spera, M., Mapelli, M., Giacobbo, N., et al. 2019, MNRAS, 485, 889
Stevens, I. R., Blondin, J. M., & Pollock, A. M. T. 1992, ApJ, 386, 265
Stone, J. M., Gardiner, T. A., Teuben, P., Hawley, J. F., & Simon, J. B. 2008, ApJS, 178, 137
Stone, J. M., Tomida, K., White, C. J., & Felker, K. G. 2020, ApJS, 249, 4
Taam, R. E., Fu, A., & Fryxell, B. A. 1991, ApJ, 371, 696
Theuns, T., Boffin, H. M. J., & Jorissen, A. 1996, MNRAS, 280, 1264
Theuns, T., & Jorissen, A. 1993, MNRAS, 265, 946
Thompson, M. J. 2006, An Introduction to Astrophysical Fluid Dynamics (London: Imperial College Press)
Tomaru, R., Done, C., Ohsuga, K., Nomura, M., & Takahashi, T. 2019, MNRAS, 490, 3098
Tout, C. A., & Eggleton, P. P. 1988, MNRAS, 231, 823
Tout, C. A., & Hall, D. S. 1991, MNRAS, 253, 9
Towns, J., Cockerill, T., Dahan, M., et al. 2014, CSE, 16, 62
van der Helm, E., Saladino, M. I., Portegies Zwart, S., & Pols, O. 2019, A&A, 625, A85
van der Walt, S., Colbert, S. C., & Varoquaux, G. 2011, CSE, 13, 22
Virtanen, P., Gommers, R., Oliphant, T. E., et al. 2020, NatMe., 17, 261
Walder, R. 1998, Ap&SS, 260, 243
Xu, W., & Stone, J. M. 2019, MNRAS, 488, 5162